36B-L RATIONALIZATION OF LIQUID/SOLID AND SOLID/SOLID INTERFACE INSTABILITIES DURING THERMAL-MECHANICAL TRANSIENTS OF METAL ADDITIVE MANUFACTURING

Katie O'Donnell, Amamchukwu Ilogebe, Maria Quintana (ISU)
Faculty: Peter Collins (ISU)
Industrial Mentor: Billy Short and Jennifer Wolk (ONR)

This project initiated in Fall 2018 and is part of a Multiple University Research Initiative (MURI) supported by ONR. The research performed during this project will serve as the basis for Ph.D. theses for Katie O'Donnell and Amamchukwu Ilogebe.

36B-L.1 Project Overview and Industrial Relevance

The length and time scales in additive manufacturing (AM), as compared to other manufacturing techniques such as welding, casting, powder metallurgy, etc., create unique relationships between the resulting thermal gradients and microstructure. The goal of this project is to understand the science behind the relation between thermal gradients in AM builds, as a function of different scan strategies, and the microstructure and texture evolution, using Ti-6Al-4V, and Inconel 738, and Haynes 282.

Understanding the underlying behavior of different AM strategies on resulting microstructure and mechanical properties of metallic printed parts can help with optimizing the final cost and mechanical properties of AM components. Another benefit of the project is the generation of data for Integrated Computational Materials Engineering (ICME) models, especially in known AM gap areas (nano and micro scale regimes of length and time).

36B-L.2 Previous Work (Work that was done since the beginning of the project, or literature review)

Past results have revealed that it is possible to vary the material state (microstructure and texture) by modifying the scanning strategy for electron beam powder bed additive manufacturing (Fig. 36B-L.1). The microstructures that are observed are consistent with those expected for Ti-6Al-4V, with a [001] growth texture in the parent beta grains, and the solid-solid phase transformation results in α laths that are consistent with the Burger's orientation relationship, as reported in [**Error! Reference source not found.-Error! Reference source not found.**]. Obtained microstructural information was used to inform on cooling rates and thermal cycle differences between the samples.

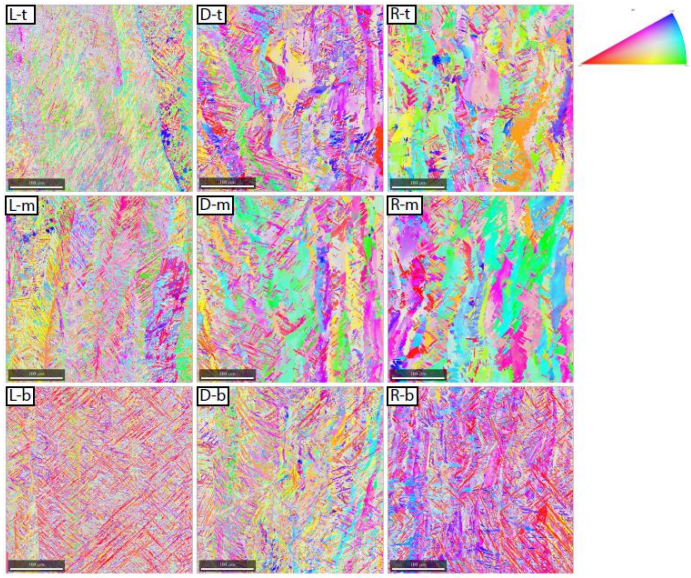

Figure 36B-L.1. Electron Backscatter Diffraction IPF-z maps of all three samples for α at the three specified locations. L – raster, D – Dehoff, R – random, t – top, m – middle and b – bottom [36B-L.6].

X-ray CT analysis of a small volume of unused powder shows the existence of internal porosity within unused powder particles, supporting the current theory that entrapped argon gas pockets likely exist in the powder. These gas pockets can be responsible for porosity observed in the parts, if the AM process (i.e., the combination of scanning strategy and processing parameters) does not fully melt the particles or does not allow for adequate convective and surface tension conditions for these gasses to escape the melt pool. The equivalent diameter of the pores measured in the parts was found to be in the ~1 µm to ~50 µm range for all three scanning strategies. Once present in the deposited material, the characteristics of the observed pores point to several interesting phenomena present in the additive manufacturing process. Characteristics of defects were analyzed, including morphological variations and surrounding microstructural and crystallographic features. Larger spherical pores, only present in the raster sample, show compression in the build direction along with horizontal sidewall perturbations (Fig. 36B-L.2) [**Error! Reference source not found.**, **Error! Reference source not found.**]. Smaller pores tended to have different geometric structures that reflected the scale of the surrounding 2-phase microstructures and were more spherical in nature.

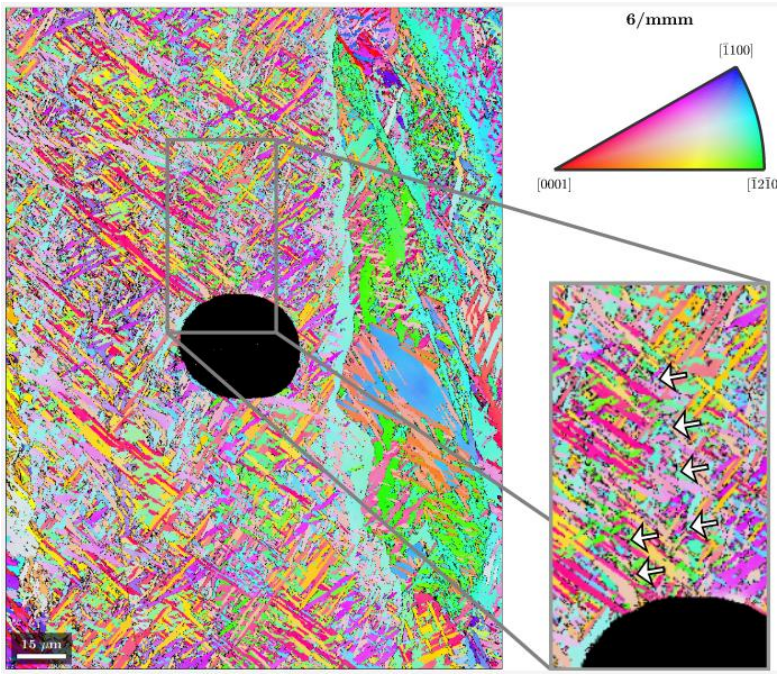

Figure 36B-L.2. EBSD of a spherical pore (sample L) close to a prior beta grain boundary, and a close up showing unindexed pixels (arrows) and slight crystallographic rotation of the alpha laths above the pore [**Error! Reference source not found.**].

Finite element modeling of spherical pores confirmed, regardless of pore size or thermal gradient used, that stress profiles on the surfaces of the pores was horizontal in nature, perpendicular to the thermal gradient/build direction, as was the case with the sidewall perturbations observed. A designed experiment with a series of models showed that the influence of the thermal gradient itself was not nearly as significant as the temperature field the pore was contained in itself. Induced compositional variations were also shown to have a noticeable effect on the resulting stress states.

EDS analysis of the samples have shown chemical variations in the material, corresponding with microstructural banding previously observed with optical microscopy [**Error! Reference source not found.**]. The variation in composition, and thus the microstructural banding, is primarily a result of preferential vaporization of aluminum from the surface of melt pools. These chemical differences have also been shown to exist across scan strategies, present in the raster sample as well as both point-melting samples in regions with and without defects. The aluminum fluctuations have also been shown to correlate with local mechanical property variations (Fig. 36B-L.3).

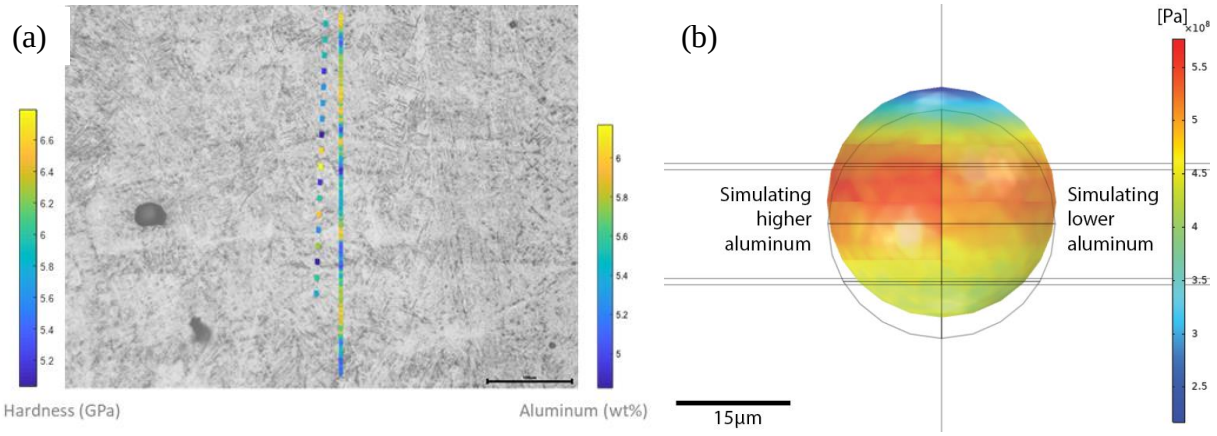

Figure 36B-L.3. An (a) optical micrograph showing a gas pore and banding corresponding to low Al bands (dark gray) and high Al bands (light gray) as well as local property variations, wherein high aluminum content corresponds with high hardness values, and (b) a two-dimensional view of the Von Mises stress distribution inside a pore generated by finite element simulation of differences in the elastic modulus in both sides of a pore as a result of chemical instabilities caused by the AM process.

Preliminary microstructural investigation into the Haynes 282 sample with cuboidal pores revealed columnar grains aligned roughly parallel to the build direction in the majority of the sample However, the microstructure above the in-built pores consisted of the nucleation of equiaxed grains, transitioning to columnar grains approximately 500µm above the cuboids (Fig. 36B-L.4). Initial research also showed the presence of carbides, as well as defects (spherical pores, lack-of-fusion defects, potential hot tearing/shrinkage porosity) throughout the build height.

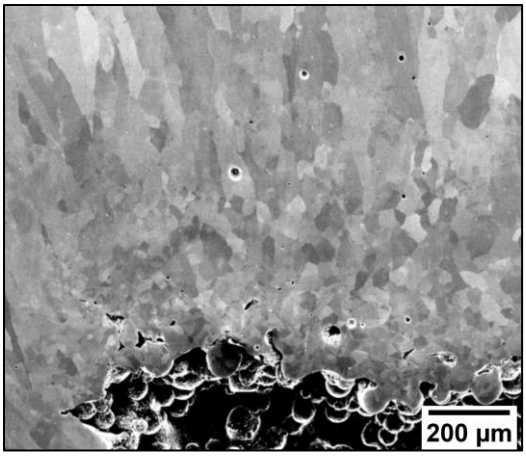

Figure 36B-L.4. Haynes 282 microstructure showing columnar grains parallel to the build direction along with an equiaxed-columnar grain transition at the top of inbuilt cuboid pore.

36B-L.3 Recent Progress (Work that has been completed since the last meeting)

Recent progress has been focused into three tasks: investigation into preferential aluminum vaporization across the scan strategies in the Ti64 builds, finite element modeling of stress and strain distributions in the presence of defects and banding in the Ti64 samples, and preliminary microstructural analysis of Haynes 282 and Inconel 738 samples.

36B-L.3.1 Compositional variations across scan strategies

Previous compositional analysis has shown evidence of aluminum vaporization and across all three samples. Further analysis revealed that the degree of preferential vaporization varied between the samples as well, with the raster sample experiencing the least aluminum loss and the random sample experiencing the greatest aluminum loss (Table

36B-L.1). However, the raster melt pools are expected to be hotter than the point-melting melt pools [36B-L.6], and, with all else being equal, should experience the most aluminum loss.

Table 36B-L.1. EDS results of aluminum variations.

	Ti	Al	V
L5, Center	90.77	5.56	3.67
L5, Edge	90.81	5.51	3.68
R5, Center	91.66	4.57	3.77
R5, Edge	91.65	4.58	3.78
D5, Center	91.36	4.86	3.78
D5, Edge	91.48	4.74	3.78

As such, recent work has focused on understanding the potential driving forces behind the aluminum loss variations between the scan strategies. There are several factors in real scenarios that are not accounted for in the case of ideal equation which can have an influence on resulting evaporation rates. Three general factors are being considered: time at temperature (as significantly high cooling rates can impair evaporation), melt pool size (as shallow melt pools will experience greater aluminum loss due to the higher surface area to volume ratio), and pressure above the melt pool.

36B-L.3.2 Finite element modeling

Finite element modeling was extended beyond spherical pores to include LOF defects modeled in the form of ellipsoids. Data from previous CT scans was used to generate model parameters and the resulting "stick model" was meant to mimic the CT scan from the edge of the raster sample, which contained the highest number of defects and therefore represented a worst-case scenario for the samples (Fig. 36B-L.5).

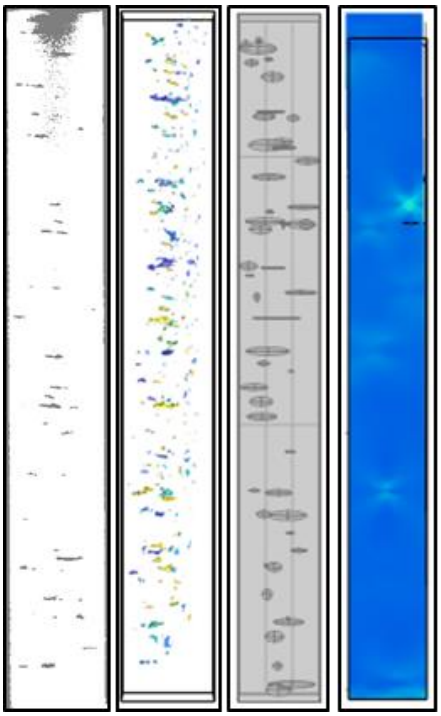

Figure 36B-L.5. Side by side images of a 2D slice from a CT dataset of the raster scan strategy, the 3D reconstruction in MIPAR, a finite element model mimicking these conditions, and the resulting stress fields.

In addition to modeling the results of tensile forces and the interaction of defects, a thermal gradient was also applied to the model by adding temperature fields to the top and bottom surfaces of the stick. As expected, the defects were shown to affect local heat flow, with the macro-scale temperature gradient decreasing directly above and below defects and increasing around the circumference of the ellipsoids in the xy-plane (Fig. 36B-L.6).

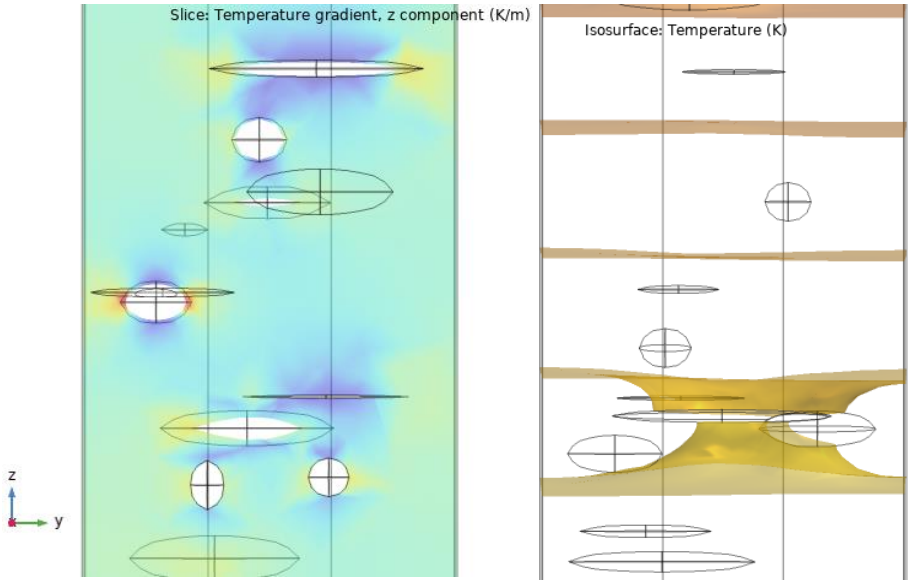

Figure 36B-L.6. Side by side images of 2D views of the stick model under a thermal gradient, with the image on the left displaying temperature gradients around defects and the image on the right displaying isotherms influenced by the presence of defects.

Compositional variations were also included in a similar model, again by varying the elastic modulus +/-5%. This new "layered" model had the same x- and y-dimensions as the previous model, but was shorter in height, to save on computation time. While the layered nature of the model did create banding of stress and strain states, these bands were overshadowed by the influence that pores had on the resulting stress and strain states, as shown in Fig. 36B-L.7.

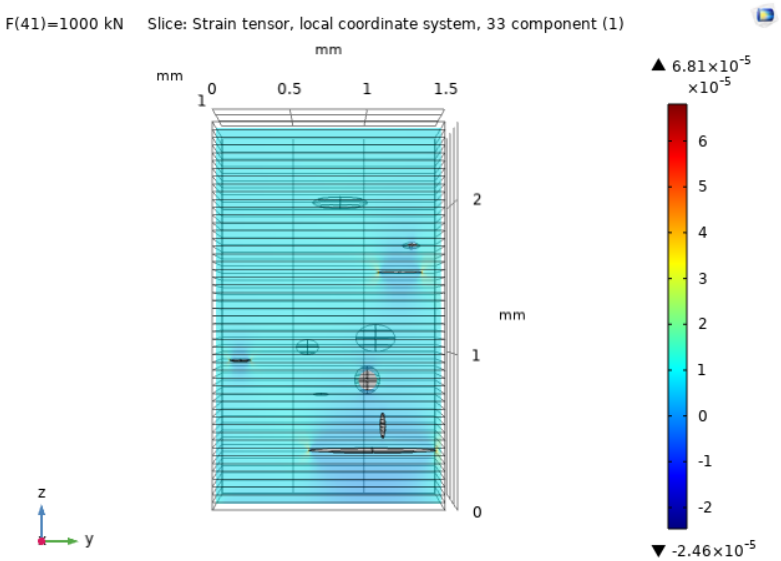

Figure 36B-L.7. The 33 component of the strain tensor after a tensile force was applied to the layered model. Banding as a result of compositional variations is not detectable at the current scale, as a result of the influence of the pores.

36B-L.3.3 Haynes 282 microstructure

The Haynes 282 sample analyzed has dimensions of 20 x 20 x 30mm, twelve inbuilt 3 x 3mm cuboidal pores, and thin wall struts of 2mm, 3mm, and 4mm at the top of the sample. Recent analysis was focused on the microstructure of the thin-walled struts. SEM images obtained from the struts showed a periodic columnar to equiaxed transition (CET) across the three struts at the same region of the build height (Fig. 36B-L.8). The distance (Z) between CETs was about 800µm, while the CET regions measured about 200µm (Z). Future work will investigate the primary driving force of the CET. The 2mm strut (Fig. 36B-L.8(b)) presents columnar grains orientated at an angle of ~30° to the build direction due to the directionality of heat flow. The columnar grains at the center of the 3mm (Fig. 36B-L.8 (b) and 4mm (Fig. 36B-L.8 (c)) struts align approximately parallel to the build direction, which is common with AM parts due to epitaxial grain growth, but are at a similar angle as the 2mm strut at the edges.

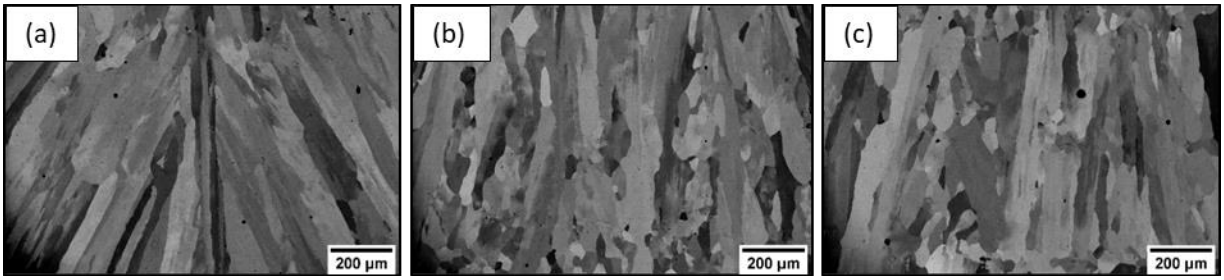

Figure 36B-L.8. Strut micrographs showing grain orientation and columnar to equiaxed transitions in the (a) 2mm strut, (b) 3mm strut, and (c) 4mm strut.

36B-L.3.4 Inconel 738 microstructure

Eight Inconel 738 (IN738) samples, 15 x 15 x 75mm, were manufactured using an electron beam process in an ARCAM Q10 Plus machine and a raster scan strategy. As part of the MURI project, ISU received a single sample from this batch. The sample was sectioned along the XZ direction parallel to the build direction (Z) to investigate the effect of thermal history on microstructure along the build height. The sectioned sample was prepared using standard metallographic procedures for nickel-based superalloys, with final polishing done in a vibratory polisher with 0.04µm colloidal silica for 24 hours. SEM images show columnar grains aligned approximately parallel to the build direction throughout the build (Fig. 36B-L-9(a)), which is associated with the directionality of the thermal gradient [**Error! Reference source not found.**, **Error! Reference source not found.**]. The average width of γ grains was measured to be 29.64 ± 6.5µm throughout the build height. There are also small regions of equiaxed grains in the sample, reported in [**Error! Reference source not found.**] from a sample from the same batch. Defects were observed throughout the sample, including spherical pores, shrinkage porosity, and lack-of-fusion defects.

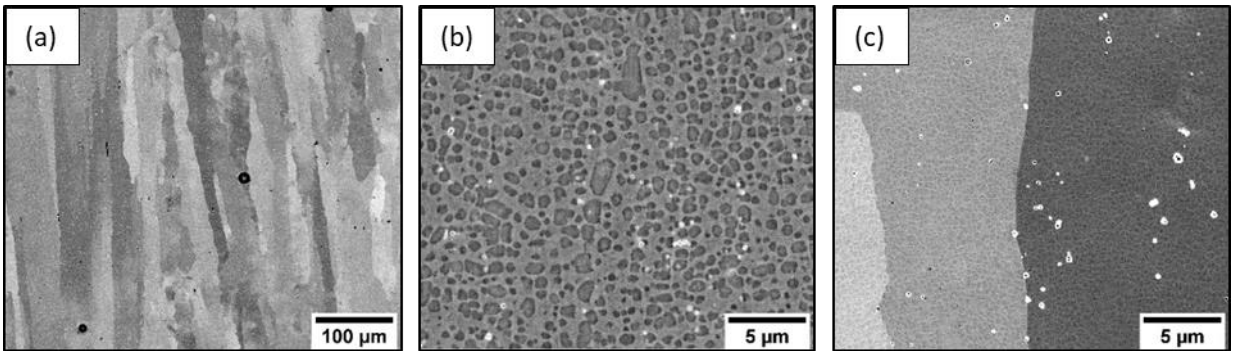

Figure 36B-L.9. EBM Inconel 738 showing (a) γ columnar grains, (b) γ' precipitates and carbides at 2mm height, and (c) γ' precipitates and carbides at 73mm height.

The distribution, size, and morphology of primary γ' precipitates were analyzed. Figures 36B-L.9(b) and 36B-L.9(c) show the primary γ' precipitates from the bottom and top of the sample, respectively. From these images, the primary γ' size decrease with height can be explained by the longer time the bottom of the sample spent at higher

temperatures and the higher number of cycles the bottom of the sample experienced compared to the top, resulting in a coarsening effect. Cuboidal γ' precipitates were observed at the bottom of the sample, whereas more spherical-shaped γ' precipitates were observed at the top. From image analysis, the primary γ' area fraction decreased by 4% with height (Fig. 36B-L.10(a)), while γ' size, measured as equivalent diameter, has a 0.40μm reduction (from 0.6 to 0.2μm) with height (Fig. 36B-L.10(b)).

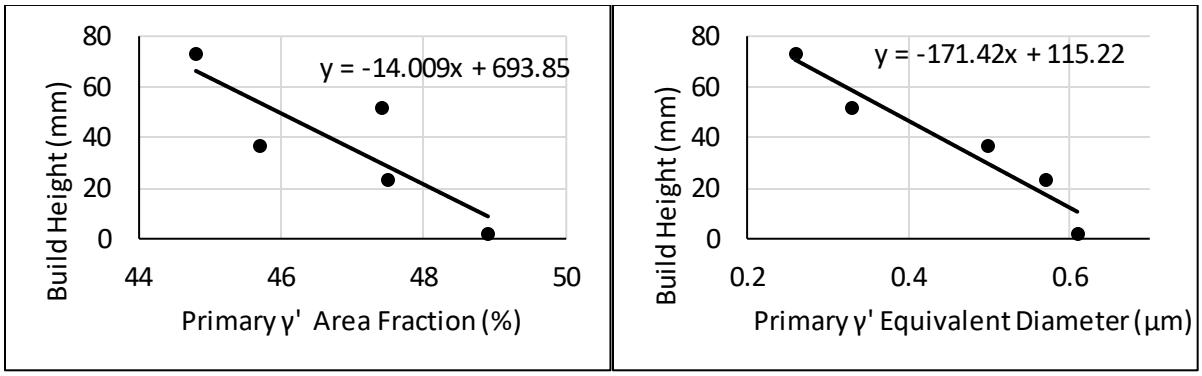

Figure 36B-L.10. Primary γ' distribution data along the build height showing (a) area fraction and (b) equivalent diameter.

Carbides of different morphology, composition, and size were observed throughout the build (Figs. 36B-L(b)-(c)), with no particular distribution. The EDS analysis of these carbides is currently ongoing.

36B-L.4 Plans for Next Reporting Period

- Examine any existing correlation, or lack of a correlation, between local property variations and local compositional variations, through nano- and micro-indentation experiments.
- Extensive literature review on driving mechanisms of aluminum vaporization with a focus on variations between the scan strategies.
- FE modeling to account for time-dependent modeling and analysis of current results.
- Finalized edits and submission of a manuscript on the Ti64 samples.
- Continue targeted polishing to bring gas pores close to the surface for EDS analysis.
- Analyze the columnar to equiaxed transition regions in the nickel-based superalloys, including using EBSD and EDS.
- Quantitative analyses of γ' precipitates to determine geometrical and height effects on distribution, shape and size for the Haynes sample.

36B-L.5 References

36B-L.1. P.L. Stephenson, N. Haghdadi, R. DeMott, X.Z. Liao, S.P. Ringer, S. Primig, Effect of scanning strategy on variant selection in additively manufactured Ti-6Al-4V, Additive Manufacturing 36 (2020) 101581.

36B-L.2. N. Haghdadi, R. DeMott, P.L. Stephenson, X.Z. Liao, S.P. Ringer, S. Primig, Five-parameter characterization of intervariant boundaries in additively manufactured Ti-6Al-4V, Materials and Design 196 (2020) 109177.

36B-L.3. M. Shao, S. Vijayan, P. Nandwana, J.R. Jinschek, The effect of beam scan strategies on microstructural variations in Ti-6Al-4V fabricated by electron beam powder bed fusion, Materials and Design 196 (2020) 109165.

36B-L.4. A.I. Saville, S.C. Vogel, A. Creuziger, J.T. Benzing, A.L. Pilchak, P. Nandwana, J. Klemm-Toole, K.D. Clarke, S.L. Semiatin, A.J. Clarke, Texture evolution as a function of scan strategy and build height in electron beam melted Ti-6Al-4V, Additive Manufacturing 46 (2021) 102118.

36B-L.5. R. DeMott, N. Haghdadi, X. Liao, S.P. Ringer, S. Primig, 3D characterization of microstructural evolution and variant selection in additively manufactured Ti-6Al-4 V, Journal of Materials Science 56 (2021) 14763–14782.
36B-L.6. M.J. Quintana, M.J. Kenney, P. Agrawal, and P.C. Collins, Texture Analysis of Additively Manufactured Ti-6Al-4V Deposited using Different Scanning Strategies, Metallurgical and Materials Transactions A: Physical Metallurgy and Materials Science 51 (2020) 6574–6583.
36B-L.7. M.J. Quintana, K.O. Donnell, M.J. Kenney, P.C. Collins, Differences in defect distribution across scan strategies in electron beam AM Ti-6Al-4V, Advanced Materials & Processes (2021) 20–23.
36B-L.8. M.J. Kenney, K. O'Donnell, M.J. Quintana, P.C. Collins, Spherical pores as 'microstructural informants': Understanding compositional, thermal, and mechanical gyrations in additively manufactured Ti-6Al-4V, Scripta Materialia 198 (2021) 113827.
36B-L.9. K. Unocic, M. Kirka, E. Cakmak, D. Greeley, A. Okello, S. Dryepondt, Evaluation of additive electron beam melting of haynes 282 alloy, Materials Science and Engineering: A 772 (2020) 138607.
36B-L.10. B. Lim, H. Chen, Z. Chen, N. Haghdadi, X. Liao, S. Primig, S.S. Babu, A.J. Breen, S.P. Ringer, Microstructure-property gradients in Ni-based superalloy (Inconel 738) additively manufactured via electron beam powder bed fusion, Additive Manufacturing 46 (2021) 102121.